J. Fluid Mech. (2009), *vol.* 629, *pp.* 1–23.
doi:10.1017/S0022112009006211 Printed in the United Kingdom

Modes in flow focusing and instability of coaxial liquid–gas jets

TING SI, FANG LI, XIE-YUAN YIN AND XIE-ZHEN YIN†

Department of Modern Mechanics, University of Science and Technology of China, Hefei, Anhui 230027, China

(Received 12 August 2008 and in revised form 18 January 2009)

Six flow modes are distinguished in the flow-focusing experiments of a liquid jet forced by a high-speed air stream. The domains of the modes are identified on the parameter space of the liquid flow rate Q_l and the gas pressure drop Δp_g. The disturbance wavelength λ and breakup length L of the jet are also measured. A theoretical model considering axisymmetric disturbances is proposed, and a basic velocity profile of hyperbolic-tangent function is utilized. The linear temporal and spatio-temporal instability analyses are carried out using the Chebyshev collocation method. The effects of the flow parameters and the velocity profile on the flow instability are discussed. The temporal instability analysis demonstrates that the interfacial shear causes the instability of short waves and retards the instability of long waves. Moreover, the spatio-temporal instability analysis gives the transition boundary between the absolute and convective instability (AI/CI). The most unstable wavelength predicted by the temporal instability analysis and the AI/CI boundary predicted by the spatio-temporal instability analysis are in good agreement with the experimental results.

1. Introduction

The breakup of a liquid jet into droplets and particles with a narrow size distribution has been increasingly attractive owing to their various applications. The applications in chemistry, medicine, biology and other subjects can be found in many papers cited by Lin (2003). Barrero & Loscertales (2007) recently reviewed some top-down methods based on capillary flows capable of producing particles down to the micrometre dimension and below. One of them is the so-called flow-focusing (FF) technique (Gañán-Calvo 1998). The flow, characterized by the formation of a steady microscopic liquid jet in the core of a high-speed gas stream, is especially advantageous for production of monodisperse sprays of micrometre size.

The geometry of the FF platform is sketched in figure 1. The FF device consists of a capillary feed tube of outer diameter D_o and inner diameter D_i and a small hole of diameter D_h in a thin plate of thickness D opening up in front of the extremity of the tube with an offset distance H. The dimensions of D_o, D_i, D_h, D and H are all submillimetre. A liquid of flow rate Q_l through the tube develops a steady cusp-like meniscus pressurized by a continuous gas supply with an extra pressure Δp_g (i.e. the difference between the pressure in the FF device and the atmospheric pressure). A thin liquid jet is issued from the vertex of the meniscus through the

† Email address for correspondence: xzyin@ustc.edu.cn

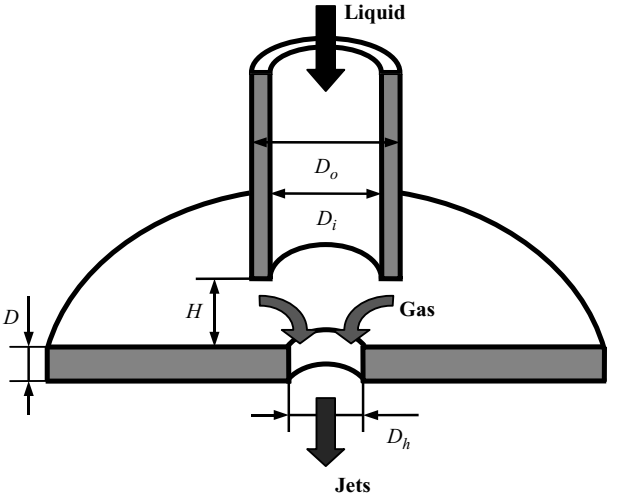

FIGURE 1. Sketch of the geometry of FF.

hole in connection with the surrounding gas. The main characters of FF have been summarized by Gañán-Calvo (1998, 1999) as follows:

(i) The gas-to-liquid momentum ratio is very close to unity in FF, i.e.

$$\frac{1}{2}\rho_1 \bar{U}_1^2 \approx \frac{1}{2}\rho_2 \bar{U}_2^2, \tag{1.1}$$

where $\bar{U}$ and ρ are the average velocity and density, and the subscripts 1 and 2 denote the liquid and gas, respectively. Note that (1.1) is determined by the simplified averaged momentum equation in the axial direction in which the viscous terms are neglected.

(ii) The diameter of the liquid jet d_1 at the orifice exit obeys the first-order scaling law of the form

$$d_1 \approx \left(\frac{8\rho_1}{\pi^2 \Delta p_g}\right)^{1/4} Q_l^{1/2}. \tag{1.2}$$

Note that for given Δp_g and Q_l, d_1 is independent of geometric parameters. Furthermore, both the viscosities $\mu_{1,2}$ and the surface tension σ hardly influence d_1. Herrada *et al.* (2008*b*) recently provided an analysis of the corrections of the jet diameter, d_1, accounting for the neglected effects of the viscosity and the surface tension. They found that expression (1.2) is in good agreement with the experimental data.

(iii) The main dimensionless parameters governing the breakup process of the liquid jet in FF are the Reynolds number, the Weber number, the density ratio and the viscosity ratio. The definitions respectively are

$$Re = \frac{\rho_1 \bar{U}_1 R_1}{\mu_1}, \quad We = \frac{\rho_1 \bar{U}_1^2 R_1}{\sigma}, \quad Q = \frac{\rho_2}{\rho_1}, \quad N = \frac{\mu_2}{\mu_1}, \tag{1.3}$$

where R_1 is the radius of the undisturbed liquid jet, $R_1 = d_1/2$. The dimensionless geometric parameters that have little influence on the process are defined as D_o/R_1, D_i/R_1, D_h/R_1, D/R_1 and H/R_1. Among the dimensionless parameters the Weber number is the most important.

It is well known that the breakup process of a liquid jet is closely associated with the instability of the jet. The jet instability considering the effects of flow parameters has been extensively investigated, through various experimental observations and theoretical instability analyses. The pioneer studies include the temporal instability analysis by Rayleigh (1878), the spatial instability analysis by Keller, Rubinow & Tu (1973) and the absolute and convective instability (AI/CI) analysis by Leib & Goldstein (1986*a*, *b*). Two different modes were distinguished: one is the Rayleigh mode (Rayleigh 1878) resulting in the formation of droplets comparable to the jet diameter in size, and the other is the Taylor mode (Taylor 1962) for which the size of droplet is much smaller than that of the jet diameter. It was also found that for uniform velocity profiles of liquid and gas the spatial instability results are in good accordance with the temporal analysis, except at sufficiently large jet velocity. Furthermore, the viscosity of the surrounding gas plays an important role in the development of jet instability. Lin & Lian (1990, 1993) and Lin & Chen (1998) investigated the linear instability of a cylindrical viscous liquid jet surrounded by a viscous gas in a circular pipe, where the basic velocity profiles of the liquid and gas satisfy exactly the Navier–Stokes equations. It was demonstrated that the mechanism of the Rayleigh mode is capillary pinching, and the mechanism of the Taylor mode is the interfacial shear and pressure fluctuation.

When disturbances propagate and amplify only downstream, it is recognized as convective instability (CI), while when disturbances propagate and amplify both downstream and upstream it belongs to absolute instability (AI). Huerre & Monkewitz (1990) reviewed the AI/CI and local/global instability of open flows. At a certain critical Weber number, the instability changes from CI into AI. Experimental and numerical studies were carried out to investigate the transition from dripping to jetting in free liquid jets and co-flowing jets. Clanet & Lasheras (1999), in their experiments in which a Newtonian fluid was injected vertically downwards into stagnant air, found a clear hysteresis effect between the transitions of dripping/jetting and jetting/dripping and further determined the corresponding critical Weber number. Sevilla, Gordillo & Martínez-Bazán (2005) studied the jetting and dripping regimes that appear in a jet of water with an air stream at the center line. Performing a linear spatio-temporal instability analysis with a uniform basic velocity profile, they concluded that the jetting phenomenon is related to CI and that the dripping regime is the consequence of a transition to AI. Lin & Lian (1993) and Lin (2003) also found that the transition from dripping to jetting is related to the AI and CI characteristic of the jet.

In spite of the complexity and special geometry in FF, to date many experimental and theoretical studies have been conducted. Experimental studies include the investigation of the scaling law of the jet diameter at the hole exit, the influence of We on the dispersion of particle size and various applications of FF in drug encapsulation, dye-labelled particles and microfluidic systems (Gañán-Calvo 1998, 1999; Martín-Banderas *et al.* 2005, 2006). Rosell-Llompart & Gañán-Calvo (2008) recently distinguished two flow regimes in FF depending on the interaction between the liquid jet and the co-flowing gas stream (e.g. the Weber number). For $1 < We < 20$ it is 'capillary flow focusing' (CFF); for $We > 20$, it turns into 'turbulent flow focusing' (TFF). As to the theoretical study, Gordillo, Pérez-Saborid & Gañán-Calvo (2001) performed a linear temporal instability analysis of an inviscid jet in FF. They obtained the basic velocity profiles of the liquid and gas by solving the Navier–Stokes equations on the slenderness approximation and explained the experimental results of atomization qualitatively. Gañán-Calvo & Riesco-Chueca (2006) studied the jetting–dripping transition of a flow-focused viscous liquid jet surrounded by a

co-flowing immiscible liquid of lower viscosity. In their spatio-temporal instability analysis, the liquids were supposed to have similar uniform axial velocity profile, and the analytical dispersion relation obtained by Funada & Joseph (2002) was adopted. The theoretical results predicted an 'elbow-like' boundary curve between the jetting–dripping transition line on the *Re–We* parameter space. The experimental results illustrated the correlation between the AI/CI transition and the onset of dripping. However, the effects of the nozzle meniscus and imperfect cylindrical jet geometry in experiments led to some distortion in the results. Herrada *et al.* (2008*b*) explored the flow patterns in FF using direct numerical simulation method. It is reported that the jetting and dripping conditions could be accurately predicted.

Recently experiments of FF relevant in producing blobs (emulsions or bubbles) based on the mircochannel device have been increasingly investigated. Extensive studies of experiments (Anna, Bontoux & Stone 2003; Gordillo *et al.* 2004; Dollet *et al.* 2008; Guillot, Colin & Ajdari 2008) and theories (Guillot *et al.* 2007; Herrada, Gañán-Calvo & Guillot 2008*a* are fulfilled. The FF flow based on the microchannel device is characterized by a confined flow with low *Re* and low *We*, where the gas or liquid is driven by a pressured liquid flow. Nevertheless, different from the FF flow concerned in this work, the hypothesis of two-dimensional flow and extremely low *Re* are often taken into account in corresponding theoretical analysis.

The great attraction between the experiments and theories motivates our interest in further studying the FF phenomenon. In this paper, we distinguish experimentally flow modes in FF and perform the temporal and spatio-temporal instability analyses of coaxial liquid–gas jets, considering viscosities of both the liquid and the gas and utilizing nearly realistic velocity profiles. The paper is structured as follows: In § 2 we distinguish experimentally the flow modes in the standard FF systems and represent their domains on the main control parameter space Q_l–Δp_g. The wavelength and breakup length of the liquid jet are measured. In § 3 we establish a theoretical model taking viscosities of both the liquid and the gas into account. The perturbed Navier–Stokes equations are linearized, and a basic velocity profile of the hyperbolic-tangent function is used. In § 4 the temporal instability analysis is performed, and the most unstable wavelength predicted by the temporal instability analysis is compared with the experimental results. In § 5 the spatio-temporal instability and the AI/CI transition are analysed. The comparison of the theoretical results with the experiments is presented. Finally main conclusions are drawn in § 6.

2. Experimental apparatus and flow modes

2.1. *Apparatus description*

A brief description of the apparatus and procedure in FF is presented. See Gañán-Calvo (1998, 1999) for more details. The experiment is carried out in an organic glass FF device with $D_i = 700$ μm, $D_o = 900$ μm, $D_h = 320$ μm, $H = 820$ μm and $D = 900$ μm (see figure 1). The mouth of the tube and the inner edge of the orifice are rounded to minimize the influence of undesirable disturbances. The focused liquid used in the experiments is water. Its density and viscosity are $\rho_1 = 998.2$ kg m^{-3} and $\mu_1 = 0.001$ Pa s at $T = 20°$C, respectively. The focusing gas is air with $\rho_2 = 1.25$ kg m^{-3} and $\mu_2 = 1.79\times10^{-5}$ Pa s at $T = 20°$C. The surface tension is $\sigma = 0.073$ N m^{-1}. (Thus the density ratio $Q \approx 0.0013$ and the viscosity ratio $N \approx 0.018$.)

The liquid is supplied by a syringe pump of flow rate ranging from 0 to 100 ml h^{-1}. The gas is forced by a gas storage. The pressure difference between the inside and outside of the FF device is measured with a conventional manometer. A stroboscope

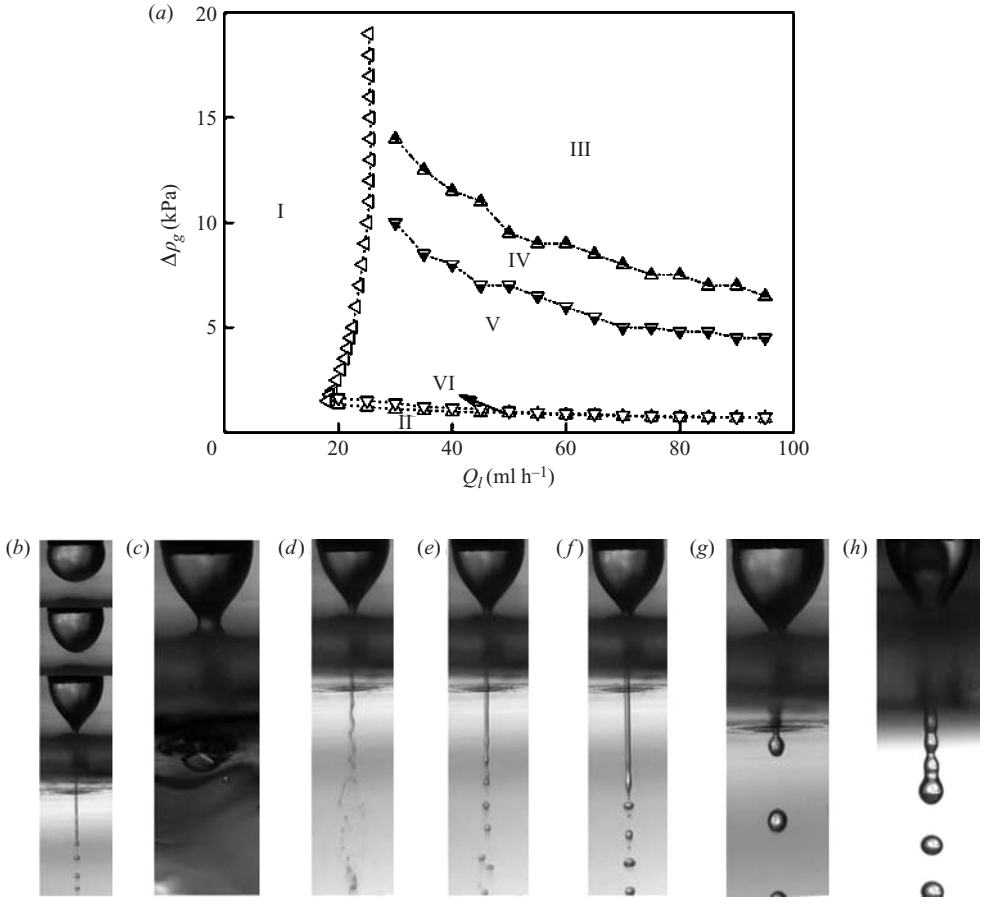

FIGURE 2. Flow modes in FF. (*a*) The domains of the modes on the Q_l–Δp_g plane with geometric parameters $D_i = 700$ μm, $D_o = 900$ μm, $D_h = 320$ μm, $H = 820$ μm and $D = 900$ μm; (*b*) cone-shaking mode in region I, $\Delta p_g = 5$ kPa, $Q_l = 10$ ml h^{-1}; (*c*) cone-adhering mode in region II, $\Delta p_g = 1$ kPa, $Q_l = 40$ ml h^{-1}; (*d*) helical jetting mode in region III, $\Delta p_g = 20$ kPa, $Q_l = 40$ ml h^{-1}; (*e*) coexisting jetting mode in region IV, $\Delta p_g = 10$ kPa, $Q_l = 40$ ml h^{-1}; (*f*) axisymmetric jetting mode in region V, $\Delta p_g = 3$ kPa, $Q_l = 40$ ml h^{-1}; (*g*) dripping mode in region VI, $\Delta p_g = 1.1$ kPa, $Q_l = 40$ ml h^{-1}; (*h*) dripping faucet, $\Delta p_g = 1.2$ kPa, $Q_l = 40$ ml h^{-1}, with $D_h = 415$ μm and $D = 500$ μm differently.

of maximum frequency of 12 kHz and a microscope combined with a CCD camera are used to capture images.

2.2. *Flow modes*

In the FF experiments, it is expected to obtain monodisperse and size-controllable droplets. As is well known, droplets produced by a liquid jet are related to the characteristic of the jet and the meniscus at the extremity of the capillary tube. In the electrospray experiments, Jaworek & Krupa (1999) and Chen *et al.* (2005) studied the spray modes and their domains. Similarly, here we observe the FF flow modes and determine their domains on the parameter plane of the liquid flow rate Q_l and the gas pressure drop Δp_g.

The flow regimes on the Q_l–Δp_g plane and the corresponding photos of the liquid jet and meniscus are shown in figure 2. The flow rate Q_l of water is below 100 ml h^{-1},

and the pressure drop Δp_g of air varies within a range of 0–20 kPa. The following FF flow modes can be observed:

(i) Cone-shaking mode. For a given pressure drop Δp_g, there is a critical flow rate Q_{lmin}, below which the meniscus pulsates periodically with an instantaneous capillary jet formed. The domain of this mode is marked with I in figure 2(*a*), and the corresponding photo is shown in figure 2(*b*). The three pictures from top to bottom in figure 2(*b*) illustrate the meniscus at different times in a period, respectively. A drop first fills up and then grows until a thin jet issues through the orifice breaking up into droplets, and ultimately the meniscus recoils. The pulse is perfectly periodic. At a fixed Δp_g, the value of Q_{lmin} is obtained by gradually increasing the flow rate Q_l from zero. As Δp_g increases the values of Q_{lmin} in the experiments first increase and then keep almost constant. The critical value Q_{lmin} is also inspected when the value of Q_l is decreased from high. The experimental results indicate that the destabilization of a stable meniscus requires a nearly equivalent critical liquid flow rate. Moreover, the critical curve is determined by the instability of the meniscus attached to the tube mouth rather than that of the liquid jet emitted from the vertex of the meniscus. As the shape of the meniscus depends strongly on the geometric parameters, the values of Q_{lmin} for the same Δp_g will be different when the geometric parameters change. The phenomenon described here is similar to the tip streaming in two-dimensional liquid–liquid FF (Anna & Mayer 2006). However, their physical mechanisms are far from the same, because the phenomenon under consideration here is caused by the tangential forcing at the interface driven by the gas sheath rather than the surfactant pollution of water surface in tip streaming. Herrada *et al.* (2008*b*) recently studied this flow pattern by direct numerical simulation and also determined the values of Q_{lmin} for the specific FF geometry.

(ii) Cone-adhering mode. For a given $Q_l (> Q_{lmin})$, there is a critical pressure drop Δp_{gmin}, below which no jet is formed, and the meniscus adheres to the entrance of the hole. As the pressure drop is too low to produce a focusing gas stream, the liquid just flows downstream along the boundary of the hole (see figure 2*c*). This mode, marked with II in figure 2(*a*), is named 'cone-adhering mode'. The value of Δp_{gmin} is obtained in the experiments by gradually decreasing the gas pressure drop Δp_g at a fixed flow rate Q_l. It can be seen that Δp_{gmin} is small and varies along a slightly descending curve as the value of Q_l increases. Furthermore, it is observed in our experiments that when the hole is broadened (e.g. D_h is larger than 500 μm), and the edge of the hole becomes far away from the meniscus, there is still a value of Δp_{gmin}, below which the meniscus becomes unstable, and the vertex of the meniscus adheres to the wall of the hole. The mode in this situation is still the cone-adhering mode.

The two modes described above only exist in FF because of its specific geometry. Moreover, these modes are closely associated with the geometric parameters (i.e. the values of Q_{lmin} and Δp_{gmin} will be different when the geometric parameters vary). Apparently, modes I and II are related to the instability of the meniscus (rather than the jet instability), which is beyond the scope of the present theoretical framework. Above the values of Q_{lmin} and Δp_{gmin}, the meniscus keeps stable all the way, and there are several other modes related to the breakup of the liquid jet. It is found in the experiments that the geometric parameters have little influence on the jet breakup as long as a stable liquid jet is formed, as demonstrated by Gañán-Calvo (1998, 1999). Therefore the main controllable parameters are Q_l and Δp_g. In our experiments, both of them can increase to very high values (e.g. $Q_l > 100$ ml h^{-1}, $\Delta p_g \gg 20$ kPa). At extremely high-pressure drop Δp_g, the liquid jet is completely atomized outside the hole, and droplets in a wide size distribution are formed. This mode is often called

'atomization mode', belonging to the TFF regime mentioned by Rosell-Llompart & Gañán-Calvo (2008). On the other hand, as the value of Q_l increases, the types of flow modes hardly vary, and only the domain of each flow mode broadens, and the transition curve of two neighboring flow modes extends. Hereinafter, the typical parameter range is adjusted to be $Q_l < 100$ ml h^{-1} and $\Delta p_g < 20$ kPa. Within this range the flow modes can be easily distinguished. Photographs of the liquid jets and steady menisci of different modes are shown in figure 2. These modes are described in the following.

(iii) Helical jetting mode. For a given $Q_l (> Q_{lmin})$, decreasing the value of Δp_g from 20 kPa first leads to a non-axisymmetric mode named 'helical jetting mode' (see figure 2*d*). The mode is denoted by III on the Q_l–Δp_g plane in figure 2(*a*). For the helical jetting mode a non-axisymmetric disturbance spreads along the liquid jet, and the jet first whips and then breaks up. Droplets formed in the high-speed air stream are elongated and split into smaller droplets. The surrounding gas stream plays an important role in the breakup of the liquid jet.

(iv) Axisymmetric jetting mode. For relatively lower values of Δp_g, an 'axisymmetric jetting mode' dominates in the breakup process of the liquid jet. For the axisymmetric jetting mode denoted by V on the Q_l–Δp_g plane in figure 2(*a*), the jet appears smooth and undisturbed near the exit of the hole. At some distance downstream wavy disturbances become visible. When the wavy amplitude becomes equal to the jet radius, the jet breaks up, and both main droplets and satellites are formed (see figure 2*f*). In this mode the liquid jet becomes thicker, and the size of main droplets is comparable to the diameter of the liquid jet.

(v) Coexisting jetting mode. Between modes III and V there is a transition mode IV, for which both non-axisymmetric and axisymmetric disturbances exist. Thus it is called 'coexisting jetting mode'. It can be seen from figure 2(*e*) that the droplets formed at the end of a straight liquid jet move downstream in a whipping way, and the diameter of droplets is nearly equivalent to that of the jet.

(vi) Dripping mode. As the value of Δp_g is decreased from the axisymmetric jetting mode, the unbroken jet is sharply shortened, and ultimately droplets are formed just at the exit of the hole. This mode, marked with VI in figure 2(*a*), is named 'dripping mode'. In this situation the satellites disappear, and the size of droplets are perfectly equal but much larger (see figure 2*g*). As the value of Δp_g is slightly decreased, droplets are formed just from the vertex of the meniscus. It should be pointed out that the dripping mode, mode VI, appears just in a narrow range of Δp_g. When the value of Δp_g is further decreased, the mode turns into the cone-adhering mode. For this reason, the hysteresis effect between the transitions of dripping/jetting and jetting/dripping in our experiments is hard to be found. Another dripping mode in the jetting to dripping process is observed occasionally. It is referred to as 'dripping faucet' (see figure 2*h*). Note that in figure 2(*h*) $D_h = 415$ μm and $D = 500$ μm, and the rest geometric parameters are the same as those in figure 2(*g*). In this situation the liquid jet outside the hole is irregularly formed and breaks up into droplets after a short distance downstream. The same phenomenon was observed in a single jet problem and studied by Clanet & Lasheras (1999).

2.3. *Disturbance wavelength and breakup length of the liquid jet*

Because of the geometric configuration, the regimes of the jet in FF are quite different from the experimental observations in Lin & Reitz (1998) in which a single jet was issued from a nozzle with a circular cross-section. They identified four regimes, the Rayleigh regime, the first wind-induced regime, the second wind-induced regime and

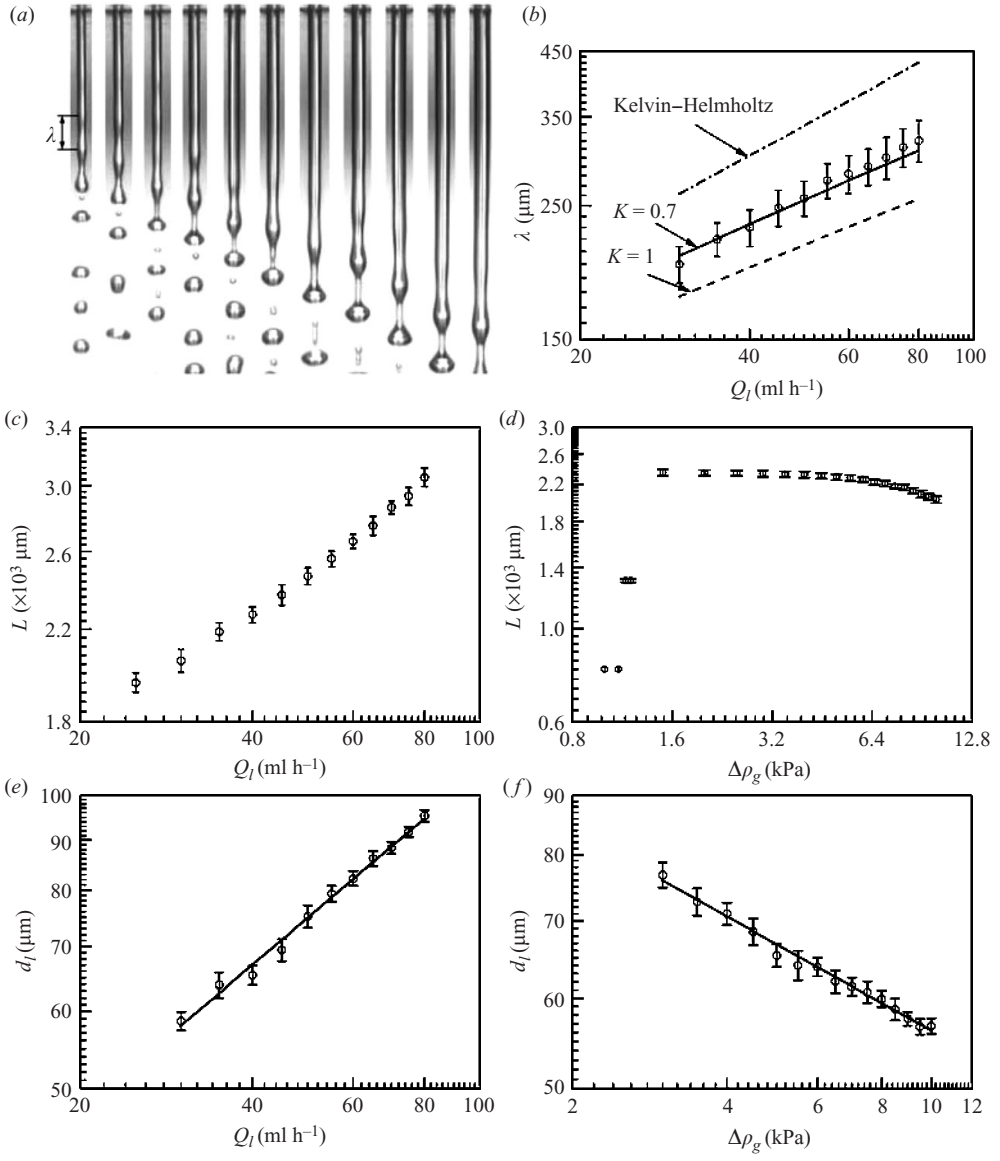

FIGURE 3. (*a*) Typical photographs of the liquid jet, (*b*) wavelength λ at the liquid surface, (*c*) breakup length L and (*e*) diameter d_1 of the jet for different values of Q_l ranging 30–80 ml h^{-1} with a step size of 5 ml h^{-1} at $\Delta p_g = 5$ kPa; (*d*)L and (*f*) d_1 for different Δp_g at $Q_l = 40$ ml h^{-1}. The continuous lines in (*b*) represent the theoretical prediction of the temporal instability analysis, and in (*e*) and (*f*) are those predicted by (1.2).

the atomization regime. In order to illuminate the difference, we collect data about the liquid jet in a range of experimental parameters, especially in the situation in which the velocity of the liquid jet is low.

The disturbance wavelength λ at the jet surface, the breakup length of the jet L defined as the distance between the tube tip and the point at which the first drop is formed and the diameter of the jet d_1 at the hole exit are measured in the experiments. Figure 3(*a*) shows the typical photographs of the liquid jet outside the

hole exit for $\Delta p_g = 5$ kPa and different values of Q_l ranging from 30 to 80 ml h^{-1} with a step size of 5 ml h^{-1}. Figure 3(*b*) shows the wavelength λ of the axisymmetric jetting mode, where the continuous lines represent the theoretical results predicted by the temporal instability analysis (see §4). The measured values of the breakup length L and diameter d_1 for different values of Q_l and given $\Delta p_g = 5$ kPa and for different values of Δp_g and given $Q_l = 40$ ml h^{-1} are shown in figures 3(*c*), 3(*e*), 3(*d*) and 3(*f*) respectively. It should be pointed out that as the breakup of the liquid jet is time-dependent, the average values with error bar of λ, L and d_1 are obtained in these figures by measuring hundreds of photographs taken by the CCD camera.

Figures 3(*e*) and 3(*f*) demonstrate that the values of the jet diameter predicted by expression (1.2) are in good agreement with the experimental data. Figures 3(*a*), 3(*b*), 3(*c*) and 3(*e*) show that as the value of Q_l increases both main droplets and satellites become large, and all values of λ, L and d_1 increase. It can also be seen from figure 3(*a*) that the shape of satellites is elongated from a sphere into a ligament for larger values of Q_l. Figure 3(*d*) indicates that for a given flow rate $Q_l = 40$ ml h^{-1} the breakup of the liquid jet undergoes different variations. For smaller values of Δp_g the flow belongs to the dripping mode, and the jet breaks up just from the vertex of the meniscus, so the breakup length of the jet in this case is kept constant approximately and equal to the length from the mouth of the capillary tube to the vertex of the meniscus. As the value of Δp_g is slightly increased, the breakup point first moves to the exit of the orifice, and then the breakup length of the liquid jet jumps to its maximum value. Note that when a dripping faucet mode exists the jump is absent, and the breakup length is rapidly increased with a small increment of Δp_g. After reaching its maximum value, the breakup length tardily decreases as the gas pressure drop Δp_g increases. Because the velocity of the liquid jet is independent of Q_l and increases as the value of Δp_g increases according to (1.1), the breakup length versus the liquid velocity behaves differently from that of a single jet case with a low jet velocity in Lin & Reitz (1998) in which the breakup length of the jet increases almost linearly as the jet velocity increases from the end of the dripping mode. It will be demonstrated in the theoretical analysis part that the main reason for this phenomenon is the significant role that the interfacial shear stress plays in the jet breakup process.

3. Theoretical model

3.1. *Formulation*

The theoretical model, similar to that of Gordillo *et al.* (2001), is sketched in figure 4. Different from the inviscid linear temporal stability analysis in Gordillo *et al.* (2001), in this study the viscous linear temporal and spatio-temporal stability analyses are performed, and the comparison with the experiments is implemented. The following assumptions are made: (i) Both the liquid and the gas are viscous, incompressible and Newtonian. (ii) The effect of the mixing layer that develops in the region in which gas velocity drops to zero is negligible. Therefore, the gas stream can be considered as a cylinder of radius R_2, and the condition at the outside surface is assumed to be slip. (iii) The effects of gravity and temperature are negligible. (iv) Only the axisymmetric disturbance is considered, i.e. the azimuthal wavenumber $n = 0$. As to the instability of non-axisymmetric disturbance and of the meniscus, further researches are required.

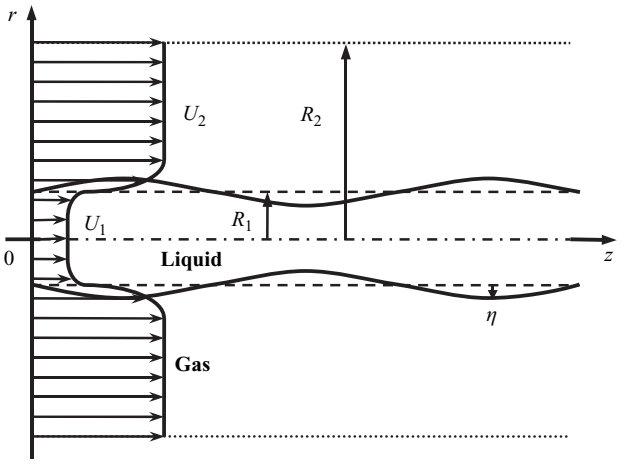

FIGURE 4. Schematic description of FF.

Besides the dimensionless parameters defined in (1.3), we introduce a new dimensionless parameter, the radius ratio

$$a = R_2/R_1. \tag{3.1}$$

Note that the characteristic scales chosen are length (R_1), velocity ($\bar{U}_1$), time ($R_1/\bar{U}_1$) and pressure ($\rho_1\bar{U}_1^2$).

The basic velocity is denoted by ($U_i(r)$, 0, 0), where the subscript $i = 1, 2$ stands for the liquid and the gas, respectively. The classical process of the normal mode method is implemented. In the cylindrical coordinates (z, r, θ), the perturbations of the axial and radial velocity components $\tilde{u}_i, \tilde{v}_i$, the pressure $\tilde{p}_i$ and the displacement of the interface $\tilde{r}$ are all decomposed into the form of a Fourier exponential, i.e.

$$(\tilde{u}_i, \tilde{v}_i, \tilde{p}_i)(z, r, t) = (u_i(r),\ v_i(r),\ p_i(r))\mathrm{e}^{\mathrm{i}(\alpha z-\omega t)},\ \tilde{r}(z, t) = \eta\mathrm{e}^{\mathrm{i}(\alpha z-\omega t)}, \tag{3.2}$$

where u_i, v_i, p_i are the amplitudes of the corresponding quantities; η is the initial disturbance amplitude on the interface; α is the wavenumber; and ω is the frequency. The governing equations are the linearized Navier–Stokes equations, i.e.

$$v_i' + \frac{1}{r}v_i + \mathrm{i}\alpha u_i = 0, \tag{3.3}$$

$$u_i'' + \frac{1}{r}u_i' - [\alpha^2 + Re_i(\mathrm{i}\alpha U_i - \mathrm{i}\omega)]u_i - Re_i v_i U_i' - \mathrm{i}\alpha Re_i p_i = 0, \tag{3.4}$$

$$v_i'' + \frac{1}{r}v_i' - \left[\frac{1}{r^2} + \alpha^2 + Re_i(\mathrm{i}\alpha U_i - \mathrm{i}\omega)\right] v_i - Re_i p_i' = 0, \tag{3.5}$$

where the prime denotes the derivative with respect to r. In (3.3)–(3.5) two different Reynolds numbers are defined as $Re_1 = Re$ and $Re_2 = Re \times Q/N$.

The boundary conditions are

$$r = 0:\ v_1 = u_1' = p_1' = 0, \tag{3.6}$$

$$r = 1:\ \mathrm{i}\omega\eta = \mathrm{i}\alpha U_1\eta - v_1, \tag{3.7}$$

$$v_1 = v_2, \tag{3.8}$$

$$u_1 - u_2 + (U_1' - U_2')\eta = 0, \tag{3.9}$$

$$\mathrm{i}\alpha v_1 + u_1' - N(\mathrm{i}\alpha v_2 + u_2') + (U_1'' - NU_2'')\eta = 0, \tag{3.10}$$

$$p_1 - \frac{2}{Re}v_1' - \left(p_2 - \frac{2N}{Re}v_2'\right) + \frac{1}{We}(1-\alpha^2)\eta = 0, \tag{3.11}$$

$$r = a\colon v_2 = u_2' = p_2' = 0, \tag{3.12}$$

where condition (3.6) expresses the axisymmetric conditions; (3.7) represents the kinematic condition at the liquid–gas interface; (3.8)–(3.11) express the continuity of the velocities and shear stress at the jet surface; and (3.12) represents the outside boundary condition at which the velocity of the gas keeps a non-zero constant value.

3.2. *Basic velocity profile*

Various basic velocity profiles were used in instability analysis. For the sake of simplicity, a uniform velocity profile with a jump at interface is often used for inviscid models (Li, Yin & Yin 2006). A piecewise linear velocity profile is more practical, but it has one or more singular points. Lin & Lian (1990) and Lin & Chen (1998) derived an analytical velocity profile satisfying the Navier–Stokes equations in their study on the coaxial pipe of viscous fluids. Gordillo *et al.* (2001) obtained the velocity profiles in the FF problem by numerically solving the boundary-layer equations. For given initial velocity profiles of liquid and gas, the evolution of the liquid and gas flows in space can be computed. However, the algebraic operation is complicated. In addition, several approximate velocity profiles, e.g. that of error function (Yecko, Zaleski & Fullana 2002) and that of hyperbolic-tangent function (Sevilla, Gordillo & Martínez-Bazán 2002), were used. In this work we utilize the velocity profile of hyperbolic-tangent function in two fluids. The basic velocity profile is assumed to be axisymmetric and unidirectional, i.e. $\boldsymbol{U}_i = U_i(r)\boldsymbol{e}_z (i = 1, 2)$, where $U_i(r)$ is the velocity component in the axial direction. In the dimensionless form $U_i(r)$ is

$$U_i(r) = a_i \tanh(b_i(r-1)) + c_i, \tag{3.13}$$

where a_i, b_i, and $c_i (i = 1, 2)$ are coefficients to be determined. The basic velocities satisfy the following conditions:

(i) continuity of the velocity and shear stress at the jet interface

$$r = 1\colon U_1 = U_2, \tag{3.14}$$

$$\frac{\mathrm{d}U_1}{\mathrm{d}r} = N\frac{\mathrm{d}U_2}{\mathrm{d}r}; \tag{3.15}$$

(ii) symmetry of the velocity at the symmetric axis,

$$r = 0\colon U_1 = 1, \tag{3.16}$$

$$\frac{\mathrm{d}U_1}{\mathrm{d}r} = 0; \text{ and} \tag{3.17}$$

(iii) the uniformity velocity at the outside boundary,

$$r = a\colon U_2 = \bar{U}_2/\bar{U}_1, \tag{3.18}$$

$$\frac{\mathrm{d}U_2}{\mathrm{d}r} = 0. \tag{3.19}$$

In terms of (1.1) and (1.3), (3.18) is written as $U_2 = Q^{-1/2}$. Equations (3.17) and (3.19) are automatically satisfied for large enough values of b_i. Therefore two unknown parameters need to be supposed. We choose the velocity at the interface Us (i.e. $Us = c_1$) and the slope of the liquid velocity profile at the interface K

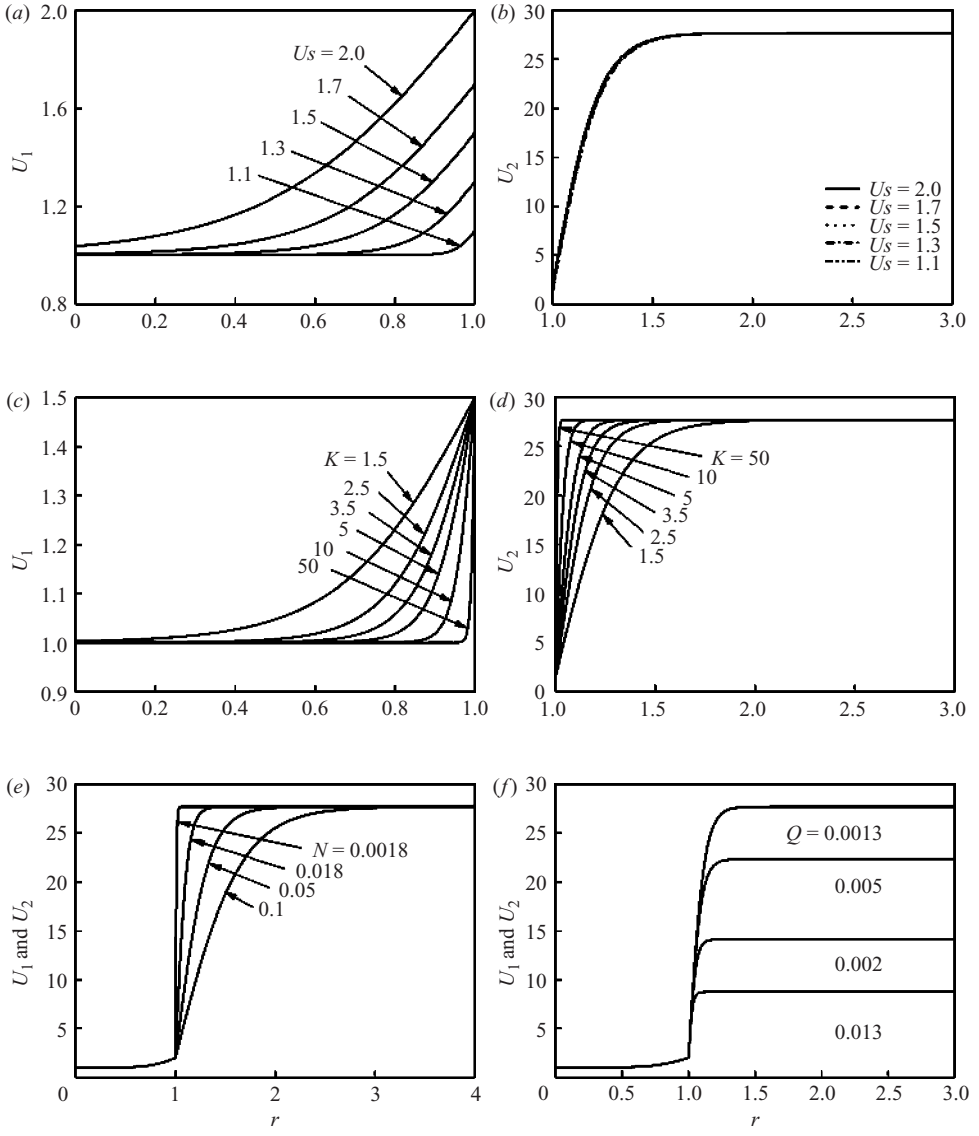

FIGURE 5. The basic velocity profiles of the liquid jet and gas stream. (*a*), (*b*) $K = 2$, $Q = 0.0013$, $N = 0.018$; (*c*), (*d*) $Us = 1.5$, $Q = 0.0013$, $N = 0.018$; (*e*) $Q = 0.0013$, $K = 4$, $Us = 2$; (*f*) $N = 0.018$, $K = 4$, $Us = 2$.

(i.e. $K = (c_1 - 1)b_1$) as controllable parameters, and $U_i(r)$ can be written as

$$U_1(r) = (Us - 1)\tanh\left[\frac{K}{Us - 1}(r - 1)\right] + Us, \tag{3.20}$$

$$U_2(r) = \left(Q^{-1/2} - Us\right)\tanh\left[\frac{K}{N\left(Q^{-1/2} - Us\right)}(r - 1)\right] + Us. \tag{3.21}$$

The conditions (3.14) and (3.15) are automatically met and (3.16) and (3.18) are approximately satisfied, because $\tanh(x) \approx 1$ for large values of x.

It can be seen from (3.20) and (3.21) that the basic velocity profiles are mainly determined by the values of K and Us. Figure 5 shows the effects of them on the

velocity profiles. For convenience, we define conventionally the liquid boundary-layer thickness Δ as $[U_1(r=1-\Delta)-Us]/(1-Us)=0.99$ and the gas boundary-layer thickness δ as $[U_2(r=1+\delta)-Us]/(\bar{U}_2/\bar{U}_1-Us)=0.99$. In the limit of $\Delta\to 0$ and $\delta\to 0$, the basic velocity profiles approximate to that of a Kelvin–Helmholtz (K-H) flow. Comparing figure 5(*a*) with figure 5(*b*), as the value of Us increases the liquid boundary-layer thickness Δ increases, while the gas boundary-layer thickness δ is kept almost constant. Figures 5(*c*) and 5(*d*) show that the values of both Δ and δ decrease as the value of K increases. In figures 5(*e*) and 5(*f*) N and Q only influence the gas stream.

As is well known, the exact basic velocity profile of FF is complicated and spatially developing. It must be obtained by direct numerical simulation of solving the evolution of the liquid–gas flow from the pressurized chamber up to the breakup point. In the present work we utilize basic velocity profile of hyperbolic-tangent function and local parallel flow approximation, which has great advantage of simplification for the instability analysis and has been demonstrated capable of predicting the experimental observations (Lin 2003; Gañán-Calvo & Riesco-Chueca 2006; Herrada *et al.* 2008*a*).

4. Temporal instability analysis

In the temporal instability analysis real wavenumber α and complex frequency $\omega=\omega_r+\mathrm{i}\omega_i$ are assumed. The eigenvalue problem in § 3.1 is solved using the Chebyshev collocation method (Lin & Chen 1998; Lin 2003). The eigenfunctions in the liquid and gas are expanded in Chebyshev polynomials. The liquid region $r\in[0,1]$ is mapped into the computational space $y\in[-1,1]$ through the linear transformation

$$r=\frac{1+y}{2}, \tag{4.1}$$

and the gas region $r\in[1,a]$ is mapped into the computational space $y\in[-1,1]$ by means of the linear transformation

$$r=\frac{y(1-a)+(1+a)}{2}. \tag{4.2}$$

Finally, a generalized eigenvalue problem is written in the form of

$$\mathrm{i}\omega[\boldsymbol{B}]\phi=[\boldsymbol{A}]\phi, \tag{4.3}$$

where the matrices $\boldsymbol{A}$ and $\boldsymbol{B}$ can be obtained from the governing equations and the boundary conditions. The corresponding dispersion relation is

$$D(\omega,\ \alpha;\ Re,\ We,\ Us,\ K,\ Q,\ N)=0. \tag{4.4}$$

A MATLAB code based on the function of *eig* is developed to solve the generalized eigenvalue problem (4.3). The validity of the code is checked by the classical results of the axisymmetric flows. The numbers of the collocation points are chosen to satisfy the desired accuracy. The sensitivity of the complex frequency (ω_r, ω_i) to the numbers of the collocation points N_1 and N_2 as well as the radius ratio a is illustrated in table 1. In the calculation $a=5$, $N_1=30$ and $N_2=60$ provide the complex frequency with a more than three-digit accuracy. Note that the radius ratio, a, is kept constant in the dispersion relation (4.4) because it hardly influences the results.

Figure 6 shows the dimensionless growth rate ω_i versus the dimensionless wavenumber α for different basic velocity profiles. The result of the K-H instability is also represented in the figure. The viscosity ratio $N=0.018$ and the density ratio

a	N_1	N_2	ω_r	ω_i
3	30	60	1.29769	0.24775
4	30	60	1.29492	0.24444
5	30	60	1.29452	0.24395
6	30	60	1.29447	0.24388
5	40	60	1.29452	0.24395
5	30	70	1.29452	0.24395

TABLE 1. Convergence of complex growth rate for different numbers of Chebyshev polynomials N_1 and N_2 and the radius ratio a; $Re = 100$, $We = 3$, $Q = 0.0013$, $N = 0.018$, $Us = 1.3$, $K = 0.7$, $\alpha = 1$.

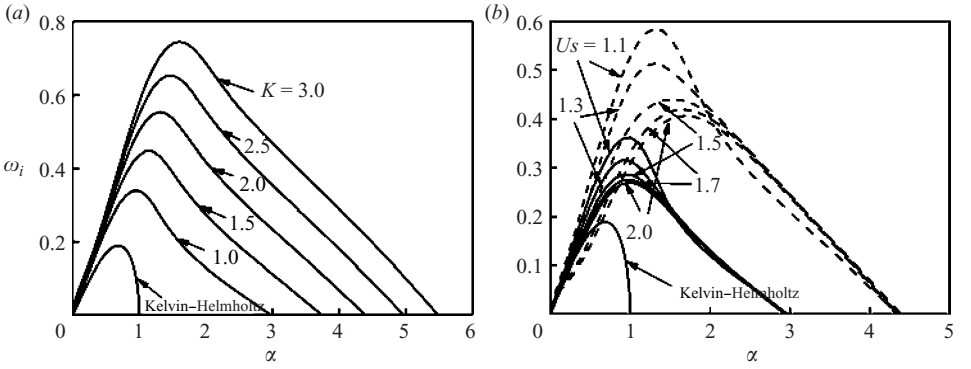

FIGURE 6. The growth rate ω_i versus the wavenumber α. (a) Effect of K with $Us = 1.2$; (b) effect of Us with the dashed lines for $K = 2$ and continuous lines for $K = 1$. The other parameters are $We = 3$, $Re = 100$, $Q = 0.0013$ and $N = 0.018$.

$Q = 0.0013$ correspond to the water–air FF experiment. As the value of K decreases, the maximum growth rate ω_{imax} and the corresponding wavenumber α_c are decreased monotonically, and moreover, the unstable region is shrunk. The jet becomes less unstable because the boundary layers become so thick that the aerodynamic effect on the instability of the jet is little (Gordillo *et al.* 2001). For thick boundary layers the capillary plays a crucial role in the jet instability. On the contrary, if the slopes of the velocity profiles are sharp, the curves deviate from the K-H instability and extend to short wavelength region. Figure 6(b) shows that the region of unstable waves is hardly changed as the value of Us increases from 1.1 to 2 for a fixed slope. Although the maximum growth rate is decreased, the corresponding wavenumber, which is larger than that of the K-H instability, varies slightly as the value of Us increases. The comparison between $K = 1$ and $K = 2$ indicates that as the value of K decreases, the effect of Us on the value of α_c becomes tiny. It is concluded that the instability of the liquid–gas flow is determined mainly by the slope of the velocity profile (i.e. the interfacial shear stress). Generally, the instability of short waves occurs at large slopes corresponding to thin boundary layer and large interfacial shear stress, while the instability of long waves occurs at small slopes. The result is accordant with Lin & Chen (1998).

The instability of the jet is influenced greatly by the Weber number and Reynolds number. Figure 7(a) shows the twofold effect of We. There is a critical wavenumber. When the wavenumber is smaller than the critical value the maximum growth rate

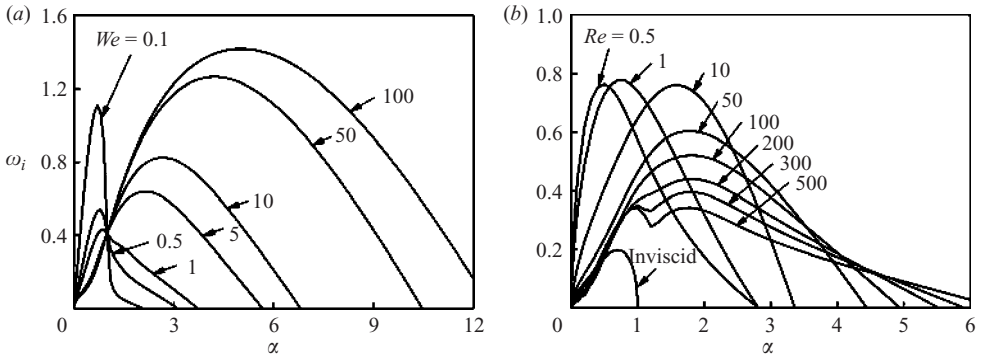

FIGURE 7. The growth rate ω_i versus the wavenumber α . (*a*) Effect of *We* with $Re = 100$; (*b*) effect of *Re* with $We = 3$. The other parameters are $Us = 1.5$, $K = 2.5$, $Q = 0.0013$ and $N = 0.018$.

decreases as the value of *We* increases, and conversely, the maximum growth rate increases. It indicates that the surface tension promotes the jet instability in the long-wavelength region and suppresses the jet instability at short wavelengths. The effect of *Re* on the instability of the jet is shown in figure 7(*b*) for given velocity profiles and a moderate Weber number. As the value of *Re* increases, the most unstable wavenumber α_c is increased rapidly, and the maximum growth rate ω_{imax} first keeps almost unchanged and then decreases until another smaller peak appears. Owing to the effect of the basic velocity profile, the curve at extremely high Reynolds number is not close to that of the inviscid case in which the most unstable wavenumber $\alpha_c = 0.697$. Generally, small *We* and moderate or small *Re*, as well as velocity profiles with small *K* and slightly moderate *Us*, favour the instability of long waves.

The theoretical predictions and the experimental results are compared on dimensional parameter space in the following. As is known, the gas pressure drop Δp_g can be estimated by the Bernoulli law, i.e.

$$\Delta p_g \approx \frac{1}{2}\rho_2 \bar{U}_2^2. \tag{4.5}$$

The mass of the liquid jet is approximately

$$Q_l \approx \pi R_1^2 \bar{U}_1. \tag{4.6}$$

Substituting (4.5) and (4.6) into (1.3), we obtain (Herrada *et al.* 2008*a*)

$$We = \frac{1}{\sigma}\left(\frac{8\rho_1 \Delta p_g^3}{\pi^2}\right)^{1/4} Q_l^{1/2}, \quad Re = \frac{2}{\mu_1}\left(\frac{\rho_1^3 \Delta p_g}{8\pi^2}\right)^{1/4} Q_l^{1/2}. \tag{4.7}$$

Apparently, the values of *We* and *Re* are determined by Q_l and Δp_g, and Δp_g affects the value of *We* more significantly. Equation (4.7) can also be written as

$$\Delta p_g = \frac{1}{2}\rho_1 \left(\frac{\sigma We}{\mu_1 Re}\right)^2, \quad Q_l = \frac{\pi(\mu_1 Re)^3}{\sigma \rho_1^2 We}. \tag{4.8}$$

The effect of Q_l on the growth rate ω_i is represented in figure 8, for two different velocity profiles $Us = 1.3, K = 1$ and $Us = 1.3, K = 0.7$. It is shown that as the value of Q_l increases the maximum growth rate ω_{imax} decreases, and the corresponding wavenumber α_c increases. As listed in table 2, the most unstable

Δp_g (kPa)	Q_l (ml h^{-1})	Re	We	K	α_c	d_1 (μm)	λ (μm)
5	30	91.59	3.97	1	1.031	57.92	176.49
5	50	118.24	5.12	1	1.094	74.78	214.74
5	80	149.66	6.48	1	1.161	94.59	255.95
5	30	91.59	3.97	0.7	0.883	57.92	206.07
5	50	118.24	5.12	0.7	0.922	74.78	254.80
5	80	149.66	6.48	0.7	0.966	94.59	307.62

TABLE 2. Theoretical prediction of the wavelength λ at the liquid jet surface.

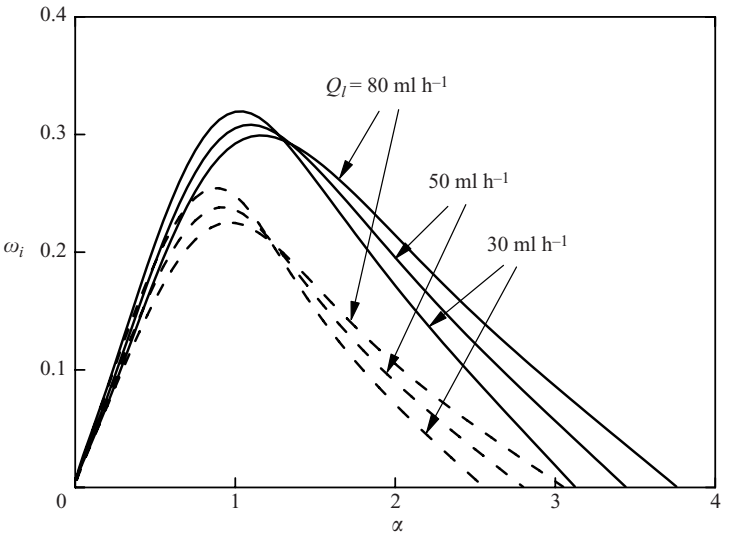

FIGURE 8. The growth rate ω_i versus the wavenumber α as Q_l varies; $\Delta p_g = 5$ kPa, $Us = 1.3$. The continuous lines are for $K = 1$, and the dashed lines are for $K = 0.7$.

wavelength $\lambda = 2\pi R_1/\alpha_c$ predicted by the temporal instability analysis, which is larger than the jet diameter, increases gradually as the value of Q_l increases. The curves of the most unstable wavelength λ versus the values of Q_l for different velocity profiles are also illustrated in figure 3(*b*). It can be seen that the wavelengths predicted for $Us = 1.3$ and $K = 0.7$ are in good agreement with the experiments.

5. Spatio-temporal instability analysis

5.1. *Approach of AI/CI*

As is well known, the flow is convectively unstable (CI) if an amplified disturbance generated by a local impulse is swept downstream or upstream away from the source; otherwise, the flow is absolutely unstable (AI) if the amplified disturbance spreads both upstream and downstream of the source and finally contaminates the entire flow domain in the limit of extremely long time. The AI/CI characteristic of the jet is determined by detecting the solutions of the dispersion relation $D(\omega, \alpha; Re, We, Us, K, Q, N) = 0$ that have zero group velocity, namely for the complex pair (α_0, ω_0),

$$\left.\frac{\partial \omega}{\partial \alpha}\right|_{\alpha_0} = 0 \quad \text{and} \quad \omega_0 = \omega(\alpha_0; Re, We, Us, K, Q, N). \tag{5.1}$$

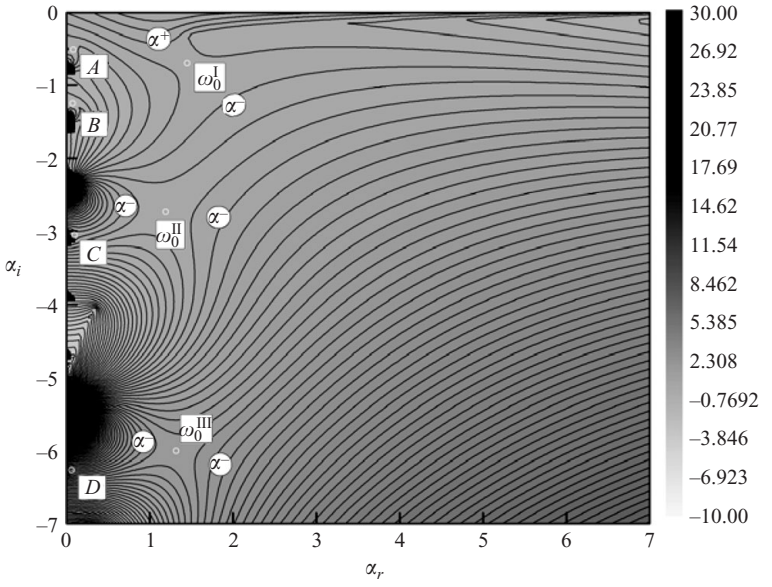

FIGURE 9. The saddle points on the complex α plane; $Re = 100$, $We = 3$, $Us = 1.2$, $K = 1.6$, $Q = 0.0013$ and $N = 0.018$.

In general, there are two distinct spatial branches of solutions of $D = 0$ on the complex α plane. The two branches will approach each other as the growth rate ω_i is decreased from large positive values, and a saddle point (or called pinching point) on the complex α plane will occur at point $\alpha = \alpha_0$. Identifying the physical and unphysical saddle points is needed. The physical saddle point must satisfy the Briggs–Bers collision criterion (Briggs 1964; Bers 1973; Huerre & Rossi 1998). According to the Briggs–Bers collision criterion the only relevant complex pair (α_0, ω_0) is the physical one if the two branches come respectively from the downstream-propagating branch $\alpha^+(\omega)$ and upstream-propagating branch $\alpha^-(\omega)$ on the complex α plane. Then if $\omega_{0i} < 0$ the flow is said to be convectively unstable, while if $\omega_{0i} > 0$, the flow is said to be absolute unstable.

A MATLAB code based on the function of *eig* is developed to solve the complex frequency ω corresponding to the complex wavenumber α for each set of parameters (Re, We, Us, K, Q, N). A typical contour plot of ω_i on the complex α plane is shown in figure 9 for $Re = 100$, $We = 3$, $Us = 1.2$, $K = 1.6$, $Q = 0.0013$ and $N = 0.018$. It can be seen that there are several saddle points. Apparently, the one at the wavenumber $\alpha_0^I = (1.483, -0.727)$ satisfies the Briggs–Bers collision criterion, and the corresponding complex frequency is $\omega_0^I = (1.412, -0.131)$. As α_i decreases, another saddle point appears at $\alpha_0^{II} = (1.152, -2.723)$, but it does not satisfy the Briggs–Bers collision criterion, as the two branches are all coming from the lower half of α plane. Similarly, the rest of the saddle points at smaller values of α_i do not satisfy the Briggs–Bers collision criterion. In addition, there are a number of saddle points close to the α_i axis, such as the points (A), (B), (C) and (D), among which the saddle points (A) and (B) satisfy the Briggs–Bers collision criterion. It must be pointed out that only the saddle point at the wavenumber α_0^I dominates the jet instability because it has the largest value of the growth rate ω_{0i} (Juniper 2006). The negative growth rate of $\omega_0^I = (1.412, -0.131)$ indicates a local CI in the situation.

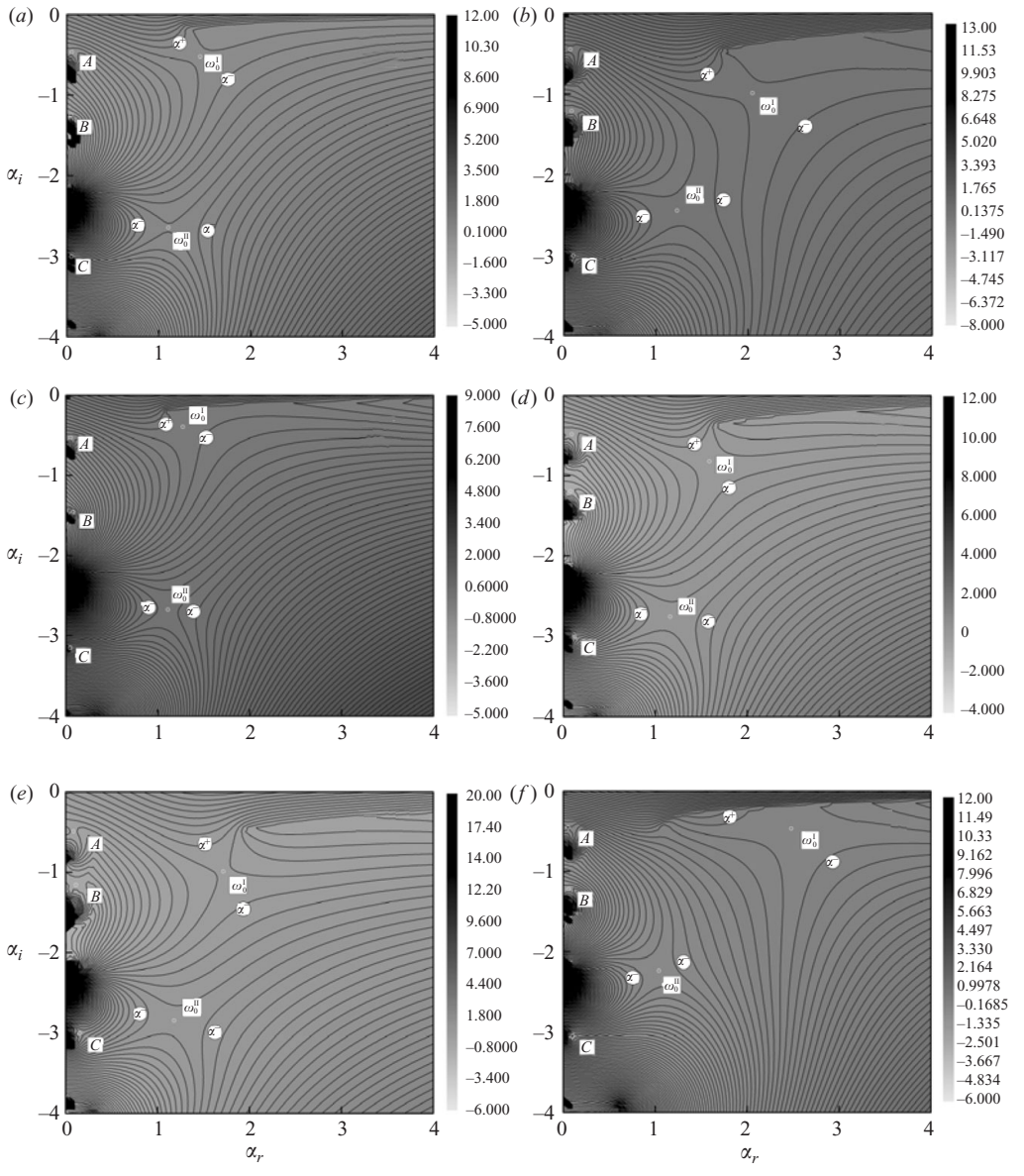

FIGURE 10. Effects of the parameters on the saddle points. (*a*) $Re = 500$; (*b*) $We = 5$; (*c*) $N = 0.05$; (*d*) $Q = 0.0026$; (*e*) $K = 3$; (*f*) $Us = 1.5$. The other parameters in the figure are the same as in figure 9.

5.2. *Effects of the physical parameters*

The saddle points vary with flow parameters (Re, We, Us, K, Q, N). Figure 10 represents six typical maps, where only the saddle point ω_0^I dominating the jet instability is considered. It can be seen from figures 10(*b*) and 10(*f*) that the Weber number and the velocity at the interface have significant influences on the position of the saddle point. As the value of We increases, ω_0^I moves away from the real and imaginary axes, and as the value of Us increases, ω_0^I moves towards larger α_r and smaller $-\alpha_i$. The effects of K and Q are similar to that of We, while the effects of Re

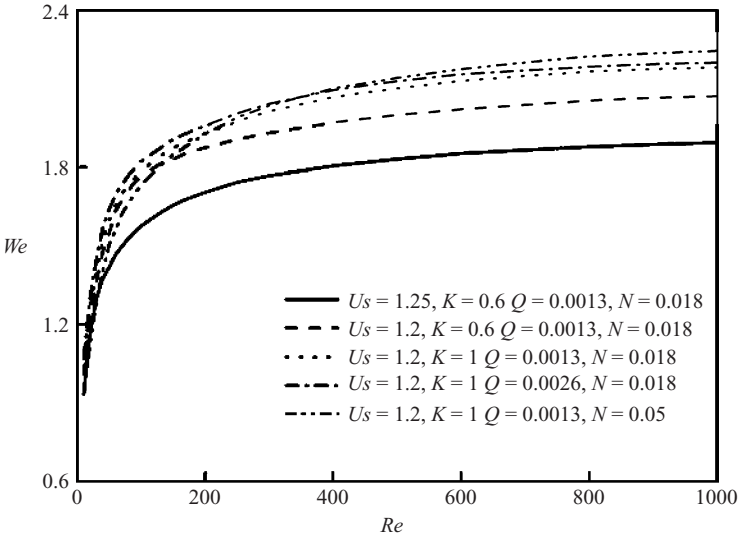

FIGURE 11. The AI/CI boundary curves on the *Re*–*We* plane.

and N are the opposite. The fact indicates that the surface tension and liquid density promote the jet instability of long waves, and the liquid viscosity, interfacial stress and velocity at the interface promote the jet instability of short waves.

The AI/CI transition boundary curves on the *Re*–*We* plane are shown in figure 11. Below the boundary curve the jet is absolutely unstable, and above it the jet is convectively unstable. It is shown that for co-flowing liquid–gas jets the transition from CI to AI takes place over a wide value range of Re and a narrow range of We. The critical Weber number changes greatly at low Reynolds numbers but changes little at high Reynolds numbers. Leib & Goldstein (1986*a*, *b*) found that the transition Weber number below which an inviscid jet is absolutely unstable is equal to π (further correction is 3.122). Our result shows that the critical value of We in the viscous case is much smaller than that in the inviscid case. From this point the interfacial shear stress plays a significant role in the formation of a convectively unstable jet.

As shown in figure 11, the transition boundary depends on the physical parameters. Firstly, the basic velocity profile affects greatly the AI/CI boundary. When the value of Us decreases slightly from 1.25 to 1.2, or the value of K decreases from 1 to 0.6, the region of AI is enlarged. The result is consistent with that of the temporal instability analysis. The effects of the density ratio Q and the viscosity ratio N are complicated. On the one hand, both Q and N influence the basic velocity profiles. On the other hand, they are involved in the momentum equations of the gas phase. Fortunately, their effects are limited and predictable. For fixed values of Us and K, the boundary moves upwards slightly as the value of Q increases; the AI region is diminished at low value of Re and is broadened at large value of Re as the value of N increases.

It should be noted that the 'elbow-like' AI/CI transition boundary in Gañán-Calvo & Riesco-Chueca (2006) does not exist in this problem. The main reason is that the parameter regions concerned are different. They considered the Reynolds number of the order of 10; however, we investigate the AI/CI transition at Re of the order of 10^2. Comparing with figure 2(*b*) in Gañán-Calvo & Riesco-Chueca (2006) for the case of a water jet in the core of air, we find that the AI/CI boundary curves tend to be coincident, though the values of the transition Weber number are slightly different

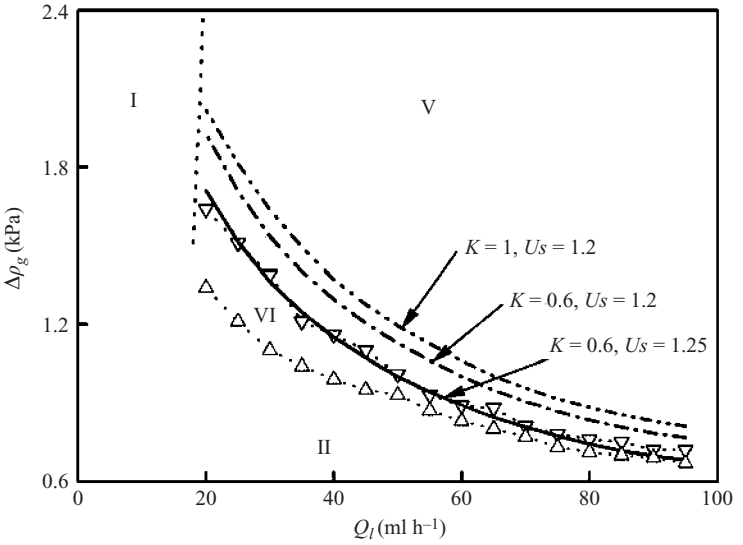

FIGURE 12. Comparison between the AI/CI boundary prediction and the experimental dripping/jetting transition on the Q_l–Δp_g plane.

for the same Reynolds number. The discrepancy may arise from the difference of the basic velocity profile.

5.3. *Comparisons with the experiments*

The AI/CI boundary curve has been calculated to discover the relation to the onset of the dripping–jetting transition in experiments (Lin & Lian 1993; Sevilla *et al.* 2005; Gañán-Calvo & Riesco-Chueca 2006). For the convenience of comparison with the experimental results, the boundary curve for $Q = 0.0013$ and $N = 0.018$ in figure 11 is redrawn on the Q_l–Δp_g plane in figure 12, where the inverse triangles stand for the boundary between the dripping modes, mode IV, and axisymmetric jetting mode, mode V, and the triangles for the transition between the dripping mode, mode IV, and cone-adhering mode, mode II. It can be seen that the AI/CI boundary curve predicted by theory approaches the experimental results as the value of K decreases from 1 to 0.6 and as the value of Us increases from 1.2 to 1.25. The curve for $K = 0.6$ and $Us = 1.25$ is in good agreement with the experiments. Hence the AI/CI instability analysis helps to understand the dripping–jetting transition in the experiments.

6. Concluding remarks

In this paper, six different flow modes of water–air FF and corresponding domains on the Q_l–Δp_g parameter plane are investigated experimentally for the specific geometry described in figure 2(*a*). Without loss of generality, the domains of them are also redrawn on the dimensionless *Re*–*We* plane (see figure 13). For relatively small values of *Re*, one can identify the cone-shaking mode, mode I, for which the meniscus pulsates periodically with an instantaneous capillary jet formed. For extremely small values of *We*, one can identify the cone-adhering mode, mode II, where no jet is formed, and the meniscus adheres to the hole. These two modes are related to the instability of the meniscus. For relatively large values of *Re* and *We*, the meniscus will keep always stable, and as the value of *We* decreases four other modes are observed sequentially, namely the helical jetting mode (III), the coexisting

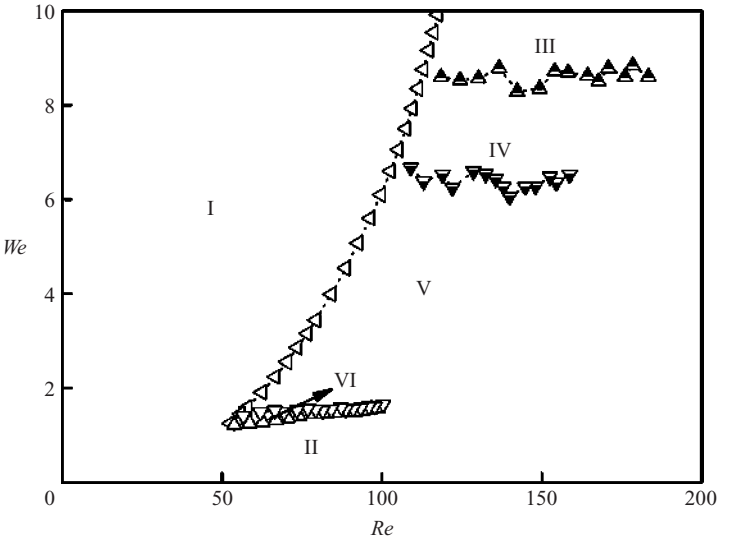

FIGURE 13. Six modes on the *Re–We* plane for the same geometric parameters as in figure 2(*a*).

jetting mode (IV), the axisymmetric jetting mode (V) and the dripping mode (VI). The Weber number is the most important parameter influencing the jetting modes (i.e. the modes III, IV and V). The critical Weber numbers between modes III/IV and V/IV are kept at approximately constant values of 8.6 and 6.4, respectively, in the range of our experiments. The dripping and jetting modes are associated closely with the instability of the co-flowing liquid–gas jets. Both the dripping mode and the axisymmetric jetting mode are caused by axisymmetric disturbances ($n = 0$), the helical jetting mode by non-axisymmetric ones ($n = 1$) and the coexisting jetting mode by both axisymmetric and non-axisymmetric ones. In this study we mainly carry out the axisymmetric instability ($n = 0$).

The linear temporal and spatio-temporal instability analyses of coaxial liquid–gas jets are performed. Both the liquid and the gas are assumed to be viscous, and the basic velocity profile is supposed to be that of hyperbolic-tangent function. The temporal instability analysis demonstrates that the interfacial shear stress plays a significant role in the jet instability; that is it enhances the instability of short waves and suppresses the instability of long waves. Moreover, the most unstable wavelength predicted is in good agreement with the experimental results quantitatively. The transition from dripping to jetting is associated with the AI/CI characteristic of the jet. The spatio-temporal instability analysis indicates that the AI/CI transition boundary curve is in good accord with the boundary curve of the dripping–jetting transition in our FF experiments.

The work was supported by the National Natural Science Foundation of China Project Nos. 10802084, 10572137.

REFERENCES

ANNA, S. L., BONTOUX, N. & STONE, H. A. 2003 Formation of dispersions using 'flow focusing' in microchannels. *Appl. Phys. Lett.* **82**, 364–67.

Anna, S. L. & Mayer, H. C. 2006 Microscale tipstreaming in a microfluidic flow focusing device. *Phys. Fluids* **18**, 121512.

Barrero, A. & Loscertales, I. G. 2007 Micro- and nanoparticles via capillary flows, *Annu. Rev. Fluid Mech.* **39**, 89–106.

Bers, A. 1973 Theory of absolute and convective instabilities. In *International Congress on Waves and Instabilities in Plasma*, Innsbruck, Austria .

Briggs, R. J. 1964 *Electron-Stream Interaction with Plasmas.* MIT Press.

Chen, X. P., Jia, L. B., Yin, X. Z. & Cheng, J. S. 2005 Spraying modes in coaxial jet electrospray with outer driving liquid. *Phys. Fluids* **17**, 032101.

Clanet, C. & Lasheras, J. C. 1999 Transition from dripping to jetting. *J. Fluid Mech.* **383**, 307–326.

Dollet, B., Hoeve, W., Raven, J-P., Marmottant, P. & Versluis, M. 2008 Role of the channel geometry on the bubble pinch-off in flow-focusing devices. *Phys. Rev. Lett.* **100**, 034504.

Funada, T. & Joseph, D. D. 2002 Viscous potential flow analysis of capillary instability. *Intl J. Multiphase Flow* **28**, 1459–1478.

Gañán-Calvo, A. M. 1998 Generation of steady liquid microthreads and micron-sized monodisperse sprays in gas streams. *Phys. Rev. Lett.* **80**, 285–288.

Gañán-Calvo, A. M. & Barrero, A. 1999 A novel pneumatic technique to generate steady capillary microjets. *J. Aerosol Sci.* **30**, 117–125.

Gañán-Calvo, A. M. & Riesco-Chueca, P. 2006 Jetting–dripping transition of a liquid jet in a lower viscosity co-flowing immiscible liquid: the minimum flow rate in flow focusing. *J. Fluid Mech.* **553**, 75–84.

Gordillo, J. M. Cheng, Z. Gañán-Calvo, A. M. Márquez, M. & Weitz, D. A. 2004 A new device for the generation of microbubbles. *Phys. Fluids* **16**, 2828–34.

Gordillo, J. M., Pérez-Saborid, M. & Gañán-Calvo, A. M. 2001 Linear stability of co-flowing liquid–gas jets. *J. Fluid Mech.* **448**, 23–51.

Guillot, P., Colin, A. & Ajdari, A. 2008 Stability of a jet in confined pressure-driven biphasic flows at low Reynolds number in various geometries. *Phys. Rev.* E **78**, 016307.

Guillot, P., Colin, A., Utada, A. S. & Ajdari, A. 2007 Stability of a jet in confined pressure-driven biphasic flows at low Reynolds number. *Phys. Rev. Lett.* **99**, 104502.

Herrada, M. A., Gañán-Calvo, A. M. & Guillot, P. 2008*a* Spatiotemporal instability of a confined capillary jet. *Phys. Rev.* E **78**, 046312.

Herrada, M. A., Gañán-Calvo, A. M., Ojeda-Monge, A., Bluth, B. & Riesco-Chueca, P. 2008*b* Liquid flow focused by a gas: jetting, dripping, and recirculation. *Phys. Rev.* E **78**, 036323.

Huerre, P. & Monkewitz, P. A. 1990 Local and global instabilities in spatially developing flows. *Annu. Rev. Fluid Mech.* **22**, 473–537.

Huerre, P. & Rossi, M. 1998 Hydrodynamic instabilities in open flows. In *Hydrodynamics and Nonlinear Instabilities* (ed. C. Godreche & P. Manneville), pp. 81–294. Cambridge University press.

Jaworek, A. & Krupa, A. 1999 Classification of the modes of EHD spraying. *J. Aerosol Sci.* **30**, 873–893.

Juniper, M. P. 2006 The effect of confinement on the stability of two-dimensional shear flows. *J. Fluid Mech.* **565**, 171–195.

Keller, J. B., Rubinow, S. I. & Tu, Y. O. 1973 Spatial instability of a jet. *Phys. Fluids* **16**, 2052–2055.

Leib, S. J. & Goldstein, M. E. 1986*a* Convective and absolute instability of a viscous liquid jet. *Phys. Fluids* **29**, 952–954.

Leib, S. J. & Goldstein, M. E. 1986*b* The generation of capillary instabilities on a liquid jet. *J. Fluid Mech.* **168**, 479–500.

Li, F. Yin, X-Y & Yin, X-Z. 2006 Instability analysis of a coaxial jet under a radial electric field in the nonequipotential case. *Phys. Fluids* **18**, 037101.

Lin, S. P. 2003 *Breakup of Liquid Sheets and Jets.* Cambridge University Press.

Lin, S. P. & Chen, J. N. 1998 Role played by the interfacial shear in the instability mechanism of a viscous liquid jet surrounded by a viscous gas in a pipe. *J. Fluid Mech.* **376**, 37–51.

Lin, S. P. & Lian, Z. W. 1990 Instability of a viscous liquid jet surrounded by a viscous gas in a vertical pipe. *J. Fluid Mech.* **218**, 641–658.

Lin, S. P. & Lian, Z. W. 1993 Absolute and convective instability of a viscous liquid jet surrounded by a viscous gas in a vertical pipe. *Phys. Fluids* A **5**, 771–773.

Lin, S. P. & Reitz, R. D. 1998 Drop and spray formation from a liquid jet. *Annu. Rev. Fluid Mech.* **30**, 85–105.

Martín-Banderas, L., Flores-Mosquera, M., Riesco-Chueca, P., Rodríguez-Gil, A., Cebolla, Á., Chávez, S. & Gañán-Calvo, A. M. 2005 Flow focusing: a versatile technology to produce size-controlled and specific morphology microparticles. *Small* **7**, 688–692.

Martín-Banderas, L., Rodríguez-Gil, A., Cebolla, Á., Chávez, S., Berdún-Álvarez, T., Fernendez-Garcia, J. M., Flores-Mosquera, M. & Gañán-Calvo, A. M. 2006 Towards high-throughput production of uniformly encoded microparticles. *Adv. Mater.* **18**, 559–564.

Rayleigh, L. 1878 On the instability of jets. *Proc. Lond. Math. Soc.* **10**, 4–13.

Rosell-Llompart, J. & Gañán-Calvo, A. M. 2008 Turbulence in pneumatic flow focusing and flow blurring regimes. *Phys. Rev.* E **77**, 036321.

Sevilla, A., Gordillo, J. M. & Martínez-Bazán, C. 2002 The effect of the diameter ratio on the absolute and convective instability of free coflowing jets. *Phys. Fluids* **14**, 3028–3038.

Sevilla, A., Gordillo, J. M. & Martínez-Bazán, C. 2005 Transition from bubbling to jetting in a coaxial air–water jet. *Phys. Fluids* **17**, 018105.

Taylor, G. I. 1962 Generation of ripples by wind blowing over viscous fluids. In *The Scientific Papers of G.I. Taylor* (ed. G. K. Batchelor), vol. 3, pp. 244–254. Cambridge University Press.

Yecko, P., Zaleski, S. & Fullana, J. M. 2002 Viscous modes in two-phase mixing layers. *Phys. Fluids* **14**, 4115–4122.